Optics Letters

# Wideband microwave electro-optic image rejection mixer

STEVEN T. LIPKOWITZ,[1,2,*] TIMOTHY U. HORTON,[2] AND THOMAS E. MURPHY[1,2]

[1]University of Maryland, College Park, Maryland 20742, USA
[2]Laboratory for Physical Sciences, College Park, Maryland 20740, USA
*Corresponding author: stl@terpmail.umd.edu

Received 31 July 2019; revised 27 August 2019; accepted 29 August 2019; posted 29 August 2019 (Doc. ID 374301); published 19 September 2019

**We present an electro-optic downconverting mixer with image rejection capabilities. By using a dual-drive Mach–Zehnder modulator (DD-MZM) to modulate an optical carrier with both a signal and a local oscillator, and an asymmetric Mach–Zehnder interferometer (AMZI) to filter the optical spectrum into two separate ports, we generate photocurrents with a phase relationship controlled via direct current (DC) bias voltage applied to the DD-MZM. By choosing these photocurrents to be in quadrature and combining them in a 90-degree electrical hybrid we achieve over 40 dB of image rejection, with a 3 dB bandwidth of approximately 20 GHz limited mainly by the AMZI free spectral range. We demonstrate downconversion of a 1 Gbaud quadrature phase-shift keyed (QPSK) signal even in the presence of a strong interfering image tone.** 

https://doi.org/10.1364/OL.44.004710

Downconversion of radio frequency (RF) signals to lower intermediate frequencies (IF) using a local oscillator (LO) is an attractive method to reduce the need for high-speed digitization at the receiver. Downconversion in the photonic domain has several advantages over electrical methods. Photonic systems are inherently more immune to electromagnetic interference than their electrical counterparts, can have substantially larger instantaneous bandwidths, and can take advantage of low-loss fiber-based transmission [1,2]. Early methods for achieving photonic downconversion make use of multiple electro-optic intensity modulators [3,4]. Newer designs incorporating multiple-phase modulators have also been reported [5], as have designs that make use of more complicated integrated devices [6]. More complicated mixer designs incorporating phase-shifting capability have also been shown [7,8]. An inherent drawback to any downconversion process is that frequencies spaced equally above and below the LO are downconverted to the same IF. One method of tackling this problem is to simply filter out frequencies that would produce images; however, this restricts the bandwidth of the system. To avoid this limitation, methods based on interferometric cancellation allow separate detection of signals above and below the LO. This technique of interferometric image rejection can be implemented by well-known electrical architectures such as those described by Hartley and Weaver [9,10]. Obtaining a pair of IF signals in quadrature is crucial to realizing the Hartley design, and electro-optic downconversion mixers that produce quadrature IF outputs have been demonstrated [11,12]. By combining quadrature outputs in a 90° electrical hybrid, interferometric image rejection is achieved. Several electro-optic downconverting mixers employing this technique have been shown [13]. Some designs make use of a duplicated input RF or LO signal that has been phase-shifted by 90° to obtain quadrature IF signals [14–16]. Other designs manipulate the IF phase via a DC bias voltage applied to an electro-optic modulator [17–19], via polarization control [20,21], or by using a 90° optical hybrid [22]. Image-rejecting downconversion of linearly chirped RF signals with instantaneous bandwidths as wide as 3 GHz has been shown [23], as has image rejecting downconversion of data modulated signals with symbol rates as high as 50 Mbaud [24].

Here we describe a new photonic downconverting mixer that uses a single Mach–Zehnder electrooptic modulator, followed by a passive fiber optic delay-line filter. The system achieves over 40 dB of image rejection at microwave frequencies. Compared to prior demonstrations, the system requires only commercially available fiber optic and electro-optic components, and in principle can be operated with only one optical bias adjustment. We demonstrate successful transmission, downconversion, and recovery of a 1 Gbaud quadrature phase-shift keyed (QPSK) signal at a carrier frequency of 27 GHz, even in the presence of a strong interfering tone at the image frequency.

Figure 1(a) shows a diagram of the system, in which the upper and lower arms of a dual-drive Mach–Zehnder modulator (DD-MZM) are driven by an RF signal $V_1 \sin(\Omega_1 t)$ and an LO $V_0 \sin(\Omega_0 t)$, respectively. The optical signal emerging from the modulator can then be described by

$$u(t) = \frac{\sqrt{P_0}}{2} e^{j\omega_0 t}[e^{j\Delta\theta} e^{jm_1 \sin \Omega_1 t} + e^{jm_0 \sin \Omega_0 t}], \tag{1}$$

where $P_0$ denotes the input laser power, $\omega_0$ is the optical carrier frequency, $m_i \equiv \pi V_i / V_\pi$ is the phase modulation amplitude (in radians) of the signal and LO, and $\Delta\theta$ is the DC bias phase of the modulator.

A bandpass filter immediately following the modulator is used to exclude all but the $\pm 1$ sidebands of the signal and

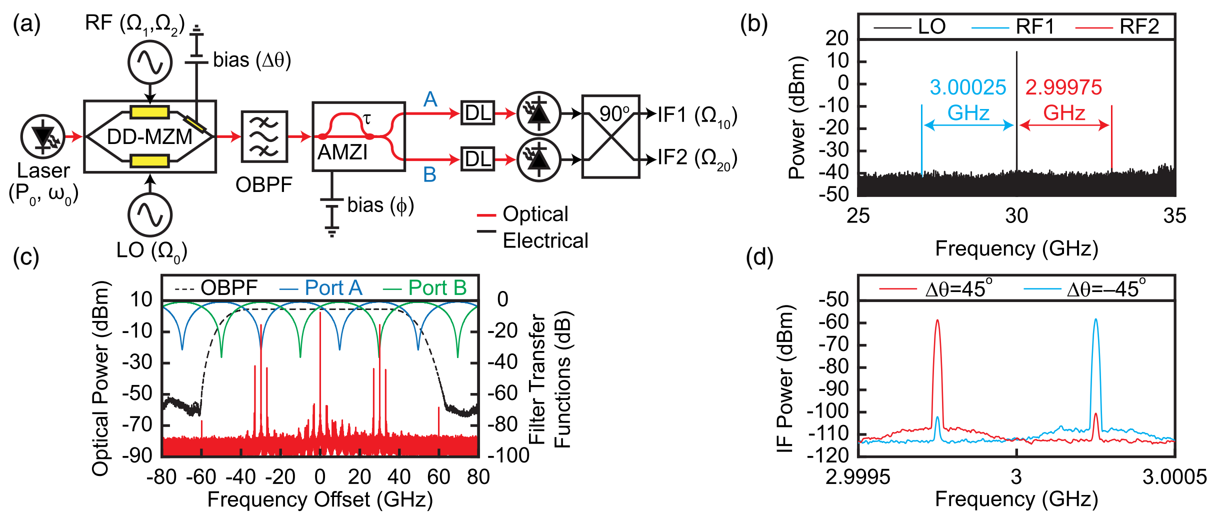


**Fig. 1.** (a) Schematic diagram of the system. (b) Measured electrical spectra of the RF and LO inputs superimposed. (c) Optical spectrum measured at the OBPF output with measured AMZI and OBPF transfer functions overlaid. (d) Output electrical spectra (averaged over 100 traces) measured after the hybrid for $\Delta\theta = 45°$ and $\Delta\theta = -45°$, showing over 40 dB of image rejection.

LO, as shown by the black-dashed curve in Fig. 1(c). The field emerging from the bandpass filter is

$$u(t) = \frac{\sqrt{P_0}}{2} e^{j\omega_0 t}\left\{ e^{j\Delta\theta}\left[1+\frac{m_1}{2}\left(e^{j\Omega_1 t}-e^{-j\Omega_1 t}\right)\right]\cdots + \left[J_0(m_0)+J_1(m_0)\left(e^{j\Omega_0 t}-e^{-j\Omega_0 t}\right)\right]\right\}, \quad (2)$$

where we have Fourier-expanded $e^{jm \sin \Omega t}$ to first order and further assumed $m_1 \ll 1$.

An asymmetric Mach–Zehnder interferometer (AMZI) delay-line filter then splits the signal into complementary output ports, with spectral transmission given by

$$t_A(\omega) = \sin\left(\frac{(\omega-\omega_0)\tau+\phi}{2}\right), \quad (3)$$

$$t_B(\omega) = \cos\left(\frac{(\omega-\omega_0)\tau+\phi}{2}\right). \quad (4)$$

The AMZI is adjusted so that the upper LO sideband emerges in port $A$ while the lower LO sideband is directed to port $B$, i.e., $t_A(\omega+\Omega_0) = t_B(\omega-\Omega_0) = 1$ as shown in Fig. 1(c). This is achieved by selecting the bias $\phi$ and free-spectral range $1/\tau$ to satisfy

$$\phi = \frac{\pi}{2}, \qquad \Omega_0\tau = \frac{\pi}{2} + 2\pi q, \quad (5)$$

where $q$ is an integer. Under this condition, the fields emerging in ports $A$ and $B$ are evaluated to be

$$u_A(t) = \frac{\sqrt{P_0}}{2} e^{j\omega_0 t}\left\{ e^{j\Delta\theta}\left[\frac{1}{\sqrt{2}} \pm \frac{m_1}{2}\left(\cos\left(\Omega_{10}\frac{\tau}{2}\right)e^{j\Omega_1 t}\cdots + \sin\left(\Omega_{10}\frac{\tau}{2}\right)e^{-j\Omega_1 t}\right)\right] + \left[\frac{J_0(m_0)}{\sqrt{2}} \pm J_1(m_0)e^{j\Omega_0 t}\right]\right\}. \quad (6)$$

$$u_B(t) = \frac{\sqrt{P_0}}{2} e^{j\omega_0 t}\left\{ e^{j\Delta\theta}\left[\frac{1}{\sqrt{2}} \mp \frac{m_1}{2}\left(\sin\left(\Omega_{10}\frac{\tau}{2}\right)e^{j\Omega_1 t}\cdots + \cos\left(\Omega_{10}\frac{\tau}{2}\right)e^{-j\Omega_1 t}\right)\right] + \left[\frac{J_0(m_0)}{\sqrt{2}} \mp J_1(m_0)e^{-j\Omega_0 t}\right]\right\}, \quad (7)$$

where $\Omega_{10} \equiv \Omega_1 - \Omega_0$, and the signs $\pm$ in the above equations depend on whether $q$ is even or odd.

When the signals $u_A$ and $u_B$ are square-law detected, the tones at $\Omega_1$ and $\Omega_0$ mix to produce a heterodyne photocurrent at the difference frequency $\Omega_{10}$,

$$i_A(t) = \frac{\mathcal{R}P_0 m_1 J_1(m_0)}{4}\cos\left(\Omega_{10}\frac{\tau}{2}\right)\cos(\Omega_{10}t+\Delta\theta), \quad (8)$$

$$i_B(t) = \frac{\mathcal{R}P_0 m_1 J_1(m_0)}{4}\cos\left(\Omega_{10}\frac{\tau}{2}\right)\cos(\Omega_{10}t-\Delta\theta), \quad (9)$$

where $\mathcal{R}$ denotes the responsivity of the photodiode, and for simplicity we have omitted the DC and higher-frequency terms. We note that Eqs. (8) and (9) hold regardless of whether $(\Omega_1 - \Omega_0)$ is positive or negative, and therefore RF signals both above and below the LO will be downconverted to the same IF band, leading to the well-known problem of image interference.

The phase of the downconverted IF signals can be controlled by adjusting the bias of the DD-MZM ($\Delta\theta$). In the special case of $\Delta\theta = \pi/4$, the outputs $i_A$ and $i_B$ will be in quadrature:

$$i_A(t') = \frac{\mathcal{R}P_0 m_1 J_1(m_0)}{4}\cos\left(\Omega_{10}\frac{\tau}{2}\right)\cos(\Omega_{10}t'), \quad (10)$$

$$i_B(t') = \frac{\mathcal{R}P_0 m_1 J_1(m_0)}{4}\cos\left(\Omega_{10}\frac{\tau}{2}\right)\sin(\Omega_{10}t'), \quad (11)$$

where $t' \equiv t + \frac{\pi}{4\Omega_{10}}$. The photocurrents $i_A$ and $i_B$ described by Eqs. (10) and (11) differ in phase by either +90° or –90°, depending on whether $\Omega_{10}$ is positive or negative. The downconverted signal and image can be distinguished by combining $i_A$

and $i_B$ in an electrical 90° hybrid coupler, which produces a single superposed output current of

$$i_{\mathrm{out}}(t') = \frac{\mathcal{R}P_0 m_1 J_1(m_0)}{2}\cos\left(\Omega_{10}\frac{\tau}{2}\right)\cos(\Omega_{10}t') \quad \mathbf{(12)}$$

that appears in either the upper or lower output port, depending on whether $\Omega_{10}$ is positive or negative.

As with any microwave photonic link, the RF to IF downconversion efficiency depends on the optical power, half-wave voltage, responsivity, and impedances. It is therefore instructive to compare the efficiency to that of a conventional nondownconverting quadrature-biased intensity-modulated RF photonic link (with the same physical parameters), for which

$$i_{\mathrm{MZM}}(t) = \frac{\mathcal{R}P_0 m_1}{2}\cos(\Omega_1 t). \quad \mathbf{(13)}$$

Relative to that of a nondownconverting link, the downconversion efficiency is

$$\frac{G}{G_{\mathrm{MZ}}} = \left[J_1(m_0)\cos\left(\Omega_{10}\frac{\tau}{2}\right)\right]^2. \quad \mathbf{(14)}$$

The optimal downconversion gain is obtained by choosing $m_0 = 1.841$, in which case Eq. (14) gives −4.95 dB for small IF frequencies.

A tunable laser set to 1552.525 nm (193.1 THz) is connected to the optical input of a DD-MZM (Sumitomo Osaka Cement T.DEH1.5-40-ADC). One or more RF signals are combined and connected to the upper port while the LO is connected to the lower port, and an adjustable DC power supply is connected to the DC bias electrode. The optical output of the DD-MZM is then passed through a programmable filter (Finisar Waveshaper 1000 s) configured as an optical bandpass filter (OBPF) with a bandwidth of 95 GHz, shown in Fig. 1(c). The output of this OBPF is then passed through an AMZI (Avensys Tech DPSK demodulator DPSK4000S30) with an FSR of $1/\tau = 40$ GHz. The AMZI and laser frequency are configured so that the unmodulated optical carrier passes equally through each output. Although the AMZI filter used in our experiment is a tunable model that accepts a DC bias voltage, athermally packaged and passively stable models are commercially available and widely used without active bias control. Each output port is then separately detected, and the two photocurrents are combined in a 90° electrical hybrid (Narda 4356B) with a nominal bandwidth of 2–18 GHz, a phase balance of ±7°, and an amplitude balance of ±0.75 dB. Optical delay lines before the detectors in each output path are used to balance the path lengths through the system that need only be equalized on a scale relative to the IF wavelength.

Figure 2(a) plots the downconversion efficiency, measured for a fixed IF frequency of 3 GHz, as a function of the LO modulation depth $m_0$, for LO frequencies of both 10 GHz and 30 GHz. These measurements were taken prior to combination in the electrical hybrid, as the output power is independent of the DD-MZM DC bias prior to combination which allows for a more stable measurement. These results are in excellent agreement with the theoretical prediction, indicated by the solid blue curve, confirming that the maximal downconversion efficiency occurs for $m_0 = 1.84$. For all subsequent measurements, the LO was set to 30 GHz and 19.5 dBm, which gives a modulation depth of $m_0 = 1.3$ radians.

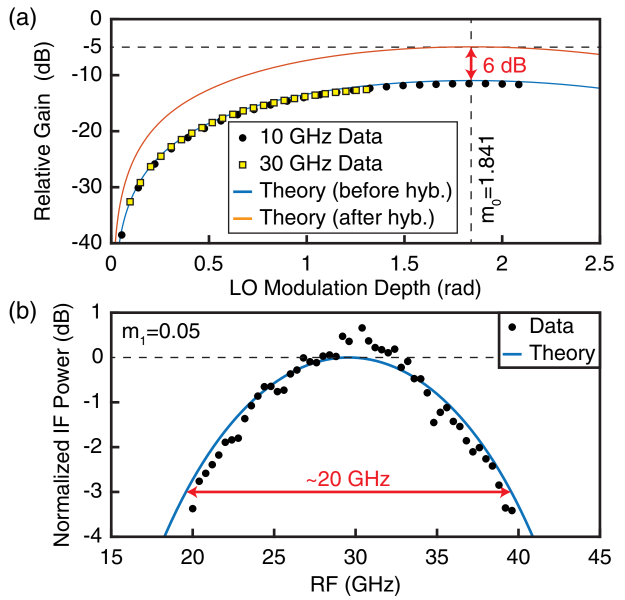


**Fig. 2.** (a) Plot of relative gain versus LO modulation depth for $f_{\mathrm{LO}} = 10$ GHz and $f_{\mathrm{LO}} = 30$ GHz in both cases $f_{\mathrm{RF}} = f_{\mathrm{LO}} + 2.99975$ GHz. (b) Normalized IF output power versus RF for $f_{\mathrm{LO}} = 30$ GHz.

Figure 2(b) plots the normalized IF output power as the RF is swept from below to above the LO. The downconversion bandwidth closely matches the expected $\cos^2(\Omega_{10}\frac{\tau}{2})$ dependence, which is constrained by the spectral shape of the AMZI filter. The 40 GHz AMZI considered here gives a 3 dB downconversion bandwidth of 20 GHz for the RF signal, although the upper and lower portions of this band are symmetrically folded into an IF bandwidth ranging from DC to 10 GHz. We expect the image reject bandwidth of the system to be limited by the specifications of the particular electrical hybrid used.

The linearity and dynamic range were evaluated by introducing two closely spaced RF tones at $f_1 = 26.99975$ GHz and $f_2 = 27.00025$ GHz, while measuring the downconverted tones ($f_1 - f_0$, $f_2 - f_0$), their third-order intermodulation products ($2f_1 - f_2 - f_0$, $2f_2 - f_1 - f_0$), and their second harmonics ($2(f_1 - f_0)$, $2(f_2 - f_0)$, $f_1 + f_2 - 2f_0$). Figure 3 plots the output power of the downconverted and spurious tones as a function of the input RF power per tone. For the parameters used here, the measured noise floor was dominated by the thermal noise of the optical receiver. The OBPF plays a critical role in suppressing the second-order distortion, which otherwise arises because of heterodyne mixing among the ±2 optical modulation sidebands. Even though the OBPF extinguishes nearly all the second-order and higher sidebands, some second-order distortion persists, which is caused by electrical crosstalk between the arms of the modulator that produces second-order optical tones at $\omega_0 \pm (2\Omega_0 - \Omega_1)$. For systems with an electrical bandwidth exceeding 4 MHz, the third-order intermodulation distortion (IMD3) dominates, and the spurious-free dynamic range is measured to be 100.6 dB.Hz$^{2/3}$.

To evaluate the image rejection performance, we employed two RF signals above and below the LO, at 26.99975 GHz and 32.99975 GHz, as shown in Fig. 1(b). Figure 1(d) plots the

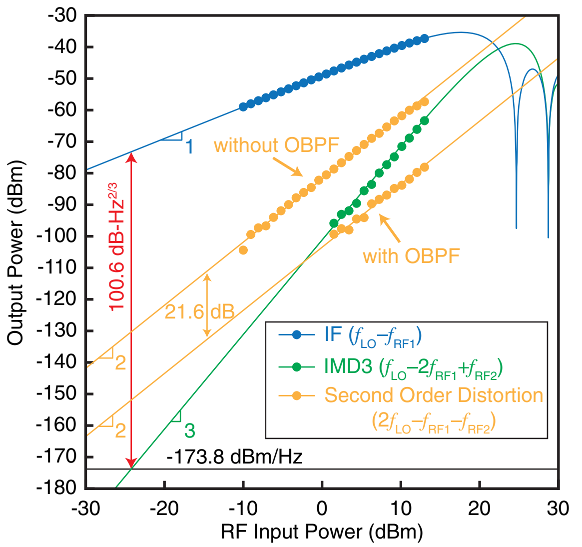


**Fig. 3.** Plot of measured spurious-free dynamic range (SFDR). The LO is at 30 GHz and 19.5 dBm. RF1 is at 26.99975 GHz, and RF2 is at 27.00025 GHz. Lines represent theoretical fits while dots represent measured data. The IF and IMD3 data were fit to theory, while the second-order distortion data were fit to lines with slope 2.

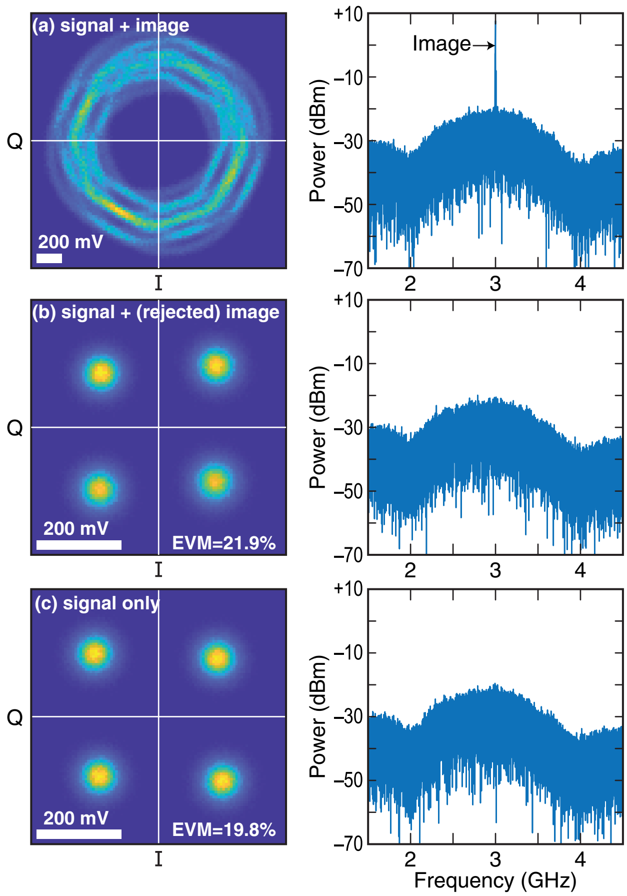


**Fig. 4.** (a) Output constellation and electrical spectrum measured (a) before the hybrid, showing large interference from the image tone, (b) after the hybrid, showing wide-band image rejection, and (c) after the hybrid when the interfering tone was turned off at the input.

corresponding IF spectrum measured after the hybrid coupler, showing over 40 dB of image rejection. Finally, we used an arbitrary waveform generator and electrical IQ mixer to produce a 1 Gbaud QPSK psuedorandom bit sequence (PRBS11) at 26.99975 GHz with average power of −10 dBm, which was combined with a stronger (0 dBm) interfering tone at 32.99975 GHz. The output of the hybrid was electrically amplified by approximately 58 dB and recorded using a spectrum analyzer and 8 GHz real time oscilloscope. The oscilloscope traces were processed offline to recover the QPSK constellation. Figure 4 shows the constellation and spectrum measured (a) prior to the hybrid coupler, where the presence of the strong interfering image tone prevents recovery of the QPSK constellation, (b) after the hybrid, where the interfering image tone is successfully cancelled and (c) the baseline response obtained by turning off the interfering tone at the input.

Here we have presented a simple electro-optic downconverting mixer that uses a single integrated DD-MZM together with optical filtering to provide image rejection. The system achieves a downconversion bandwidth of 20 GHz and is capable of over 40 dB of image rejection. We further demonstrate that 1 Gbaud QPSK data can be separated from a strong interfering image tone with only minor degradation.

## REFERENCES


1. J. Capmany and D. Novak, Nat. Photonics **1**, 319 (2007).
2. A. J. Seeds, IEEE Trans. Microw. Theory Tech. **50**, 877 (2002).
3. G. K. Gopalakrishnan, R. P. Moeller, M. M. Howerton, W. K. Burns, K. J. Williams, and R. D. Esman, IEEE Trans. Microw. Theory Tech. **43**, 2318 (1995).
4. J. Gallo and J. Godshall, IEEE Photon. Technol. Lett. **10**, 1623 (1998).
5. V. R. Pagán, B. M. Haas, and T. E. Murphy, Opt. Express **19**, 883 (2011).
6. Z. Tang, F. Zhang, D. Zhu, X. Zou, and S. Pan, in *International Topical Meeting on Microwave Photonics (MWP)* (2013), pp. 150–153.
7. T. Jiang, R. Wu, S. Yu, D. Wang, and W. Gu, Opt. Express **25**, 4519 (2017).
8. T. Jiang, S. Yu, R. Wu, D. Wang, and W. Gu, Opt. Lett. **41**, 2640 (2016).
9. A. A. Abidi, IEEE J. Solid-State Circuits **30**, 1399 (1995).
10. B. Razavi, IEEE Trans. Circuits Syst. II Analog Digit. Signal Process. **44**, 428 (1997).
11. V. R. Pagán and T. E. Murphy, Opt. Lett. **40**, 2481 (2015).
12. J. Li, J. Xiao, X. Song, Y. Zheng, C. Yin, Q. Lv, Y. Fan, F. Yin, Y. Dai, and K. Xu, Chin. Opt. Lett. **15**, 010014 (2017).
13. D. Zhu and S. Pan, Photonics **5**, 6 (2018).
14. L. Chao, C. Wenyue, and J. F. Shiang, IEEE Trans. Microw. Theory Tech. **45**, 1478 (1997).
15. J. Zhang, E. H. W. Chan, X. Wang, X. Feng, and B. Guan, IEEE Photon. J. **8**, 13900411 (2016).
16. Z. Shi, S. Zhu, M. Li, N. H. Zhu, and W. Li, Opt. Commun. **428**, 131 (2018).
17. Z. Tu, A. Wen, W. Zhang, Z. Xiu, and G. Yu, Opt. Commun. **430**, 158 (2019).
18. Y. Gao, A. Wen, W. Chen, and X. Li, Opt. Lett. **42**, 1105 (2017).
19. S. T. Lipkowitz, T. U. Horton, V. R. Pagán, and T. E. Murphy, in *International Topical Meeting on Microwave Photonics (MWP)* (2018).
20. Y. Gao, A. Wen, W. Jiang, Y. Fan, and Y. He, Opt. Express **26**, 7336 (2018).
21. P. Li, W. Pan, X. Zou, B. Lu, L. Yan, and B. Luo, IEEE J. Quantum Electron. **53**, 9100208 (2017).
22. Z. Tang and S. Pan, Opt. Lett. **42**, 33 (2017).
23. D. Zhu, W. Chen, and S. Pan, Opt. Express **26**, 28022 (2018).
24. Z. Tang and S. Pan, J. Lightwave Technol. **34**, 4729 (2016).